Check for updates

ADVANCED MATERIALS
www.advmat.de

High Entropy Alloys Enable Durable and Efficient Lithium-Mediated CO_2 Redox Reactions

Liang Sun, Jodie A. Yuwono, Shilin Zhang, Biao Chen, Guanjie Li, Huanyu Jin, Bernt Johannessen, Jianfeng Mao, Chaofeng Zhang,* Muhammad Zubair, Nicholas Bedford, and Zaiping Guo**

Designing electrocatalysts with high activity and durability for multistep reduction and oxidation reactions is challenging. High-entropy alloys (HEAs) are intriguing due to their tunable geometric and electronic structure through entropy effects. However, understanding the origin of their exceptional performance and identifying active centers is hindered by the diverse microenvironment in HEAs. Herein, NiFeCoCuRu HEAs designed with an average diameter of 2.17 nm, featuring different adsorption capacities for various reactants and intermediates in Li-mediated CO_2 redox reactions, are introduced. The electronegativity-dependent nature of NiFeCoCuRu HEAs induces significant charge redistribution, shifting the *d*-band center closer to Fermi level and forming highly active clusters of Ru, Co, and Ni for Li-based compounds adsorptions. This lowers energy barriers and simultaneously stabilizes *$LiCO_2$ and $LiCO_3$+CO intermediates, enhancing the efficiency of both CO_2 reduction and Li_2CO_3 decomposition over extended periods. This work provides insights into specific active site interactions with intermediates, highlighting the potential of HEAs as promising catalysts for intricate CO_2 redox reactions.

1. Introduction

The efficient utilization or fixation of CO_2 into chemical products through electrocatalytic reductions is crucial for maintaining the global carbon balance.[1] Prevailing CO_2 fixation strategies for products like CO, CH_4, C_2H_4, HCOOH, etc. may require additional energy-intensive compression or liquefaction processes for transportation and storage.[2] Alternatively, a promising approach for either CO_2 fixation to solid chemicals or energy storage includes Li-CO_2 batteries (LCBs), where CO_2 serves as an energy carrier, enabling reversible storage and release of renewable energy through the following reaction: $4Li^+ + 3CO_2\,(g) + 4e^- \leftrightarrow 2Li_2CO_3\,(s) + C\,(s)$. However, the dominant CO_2 reduction and evolution involve multistep reactions and multielectron transfers with elusive intermediates, complicating the battery systems. The decomposition of insulating Li_2CO_3 discharge product during CO_2 evolution presents particular challenges in the reversibility, cycling, and energy efficiency of LCBs.[3] Therefore, it is imperative to develop electrodes with bidirectional catalysts that facilitate both the reduction of CO_2 and the decomposition of discharge products. To address the challenges, various catalysts such as carbon-based materials, transition metals compound catalysts, and noble metals catalysts have been employed.[4] They play crucial roles in facilitating the

L. Sun, J. A. Yuwono, S. Zhang, G. Li, H. Jin, J. Mao, Z. Guo
School of Chemical Engineering
The University of Adelaide
Adelaide 5000, Australia
E-mail: shilin.zhang01@adelaide.edu.au; zaiping.guo@adelaide.edu.au

B. Chen
School of Materials Science and Engineering and Tianjin Key Laboratory of Composite and Functional Materials
Tianjin University
Tianjin 300350, China

The ORCID identification number(s) for the author(s) of this article can be found under https://doi.org/10.1002/adma.202401288

© 2024 The Authors. Advanced Materials published by Wiley-VCH GmbH. This is an open access article under the terms of the Creative Commons Attribution-NonCommercial License, which permits use, distribution and reproduction in any medium, provided the original work is properly cited and is not used for commercial purposes.

DOI: 10.1002/adma.202401288

B. Johannessen
Australian Synchrotron
ANSTO, 800 Blackburn Rd, Clayton, VIC 3168, Australia

B. Johannessen
Institute for Superconducting & Electronic Materials
University of Wollongong
Wollongong, NSW 2500, Australia

C. Zhang
Institutes of Physical Science and Information Technology
Anhui University
Hefei 230601, China
E-mail: cfz@ahu.edu.cn

M. Zubair, N. Bedford
School of Chemical Engineering
UNSW Sydney, Sydney 2052, Australia

decomposition of Li_2CO_3 and accelerating the CO_2 reduction, thereby reducing overpotential and improving the cycling life of the LCBs. However, it is important to note that many of the reported LCBs still encounter challenges such as high charged potential plateau and short cycle performance.[4b]

Noble metals are pivotal in heterogeneous catalysis, influencing the production of numerous industrial chemicals.[5] For example, Pt exhibits advantages in de-/hydrogenation, Ag is efficient to catalyze the epoxidation of ethylene, Pd is renowned for carbon-carbon coupling, and Ru promotes the formation of carbon–heteroatom (such as N, O, P and S) bonds.[5a] This is because of their excellent capacity to function as electron donors and acceptors, enabling them to catalyze both reduction and oxidation reactions that include a few proton/electron transfer processes. However, mono- or bimetallic-noble catalysts cannot fulfill all the requirements for complex reactions, which contain multiple proton/electron transfer processes involving various reactants and intermediate species.[4e,6] The limitation is due to the most favorable adsorption sites for different species should be different. Therefore, it is reasonable to assume that designing a catalyst with a variety of adsorption sites could significantly promote complex reactions.

High entropy alloys (HEAs), in which at least five principal elements (with each elemental ratio between 5 and 35 at. %) mix randomly, have emerged as catalysts over the past decade.[7] The intriguing interactions among multiple principal atoms, including factors such as mixing entropy, mixing enthalpy, difference in atomic size, electronegativity, and valence electron concentration, endow HEAs with unique chemical compositions, electronic structure and atomic spatial arrangements compared with conventional dilute alloys.[8] HEAs possess distinctive physicochemical properties that render them promising candidates for catalytic applications, including the hydrogen evolution reaction, hydrogen oxidation reaction, oxygen reduction reaction, oxygen evolution reaction, and carbon dioxide reduction reaction.[9] With appropriate element numbers, species, and concentrations, HEAs with multiple adsorption and catalytical sites are expected to meet the requirements of CO_2 reduction and evolution reactions (CRR/CER). Exploring HEAs is of great interest for both the elemental understanding of the origin of outstanding performance and the active sites of intermetallic compounds in energy conversion systems.

Here, guided by theoretical predictions, we present the rational design of NiFeCoCuRu HEAs with an average diameter of 2.17 nm as bifunctional catalyst for Li-mediated CO_2 redox reactions (**Figure 1a**). Combining experimental and theoretical results, NiFeCoCuRu HEAs exhibit significant charge redistribution, influenced by electronegativity-dependent characteristics of five elements. We observed that NiFeCoCuRu HEAs, featuring a *d*-band center closer to Fermi level and active clusters of Ru, Co, and Ni, simultaneously stabilizes $*LiCO_2$ and $LiCO_3$+CO intermediates, enabling a durable CO_2 redox for over 2900 h with a low overpotential of 0.82 V, as compared with pure Ru metals with an equiv. metal loading on Ketjen black (KB). Our work highlights the potential of HEAs as promising catalysts for CO_2 redox reactions involving multiple steps and provides fundamental understanding of the origin of outstanding performance.

2. Results and Discussion

A survey of previously developed catalysts for LCBs reveals that transition metals, such as Fe, Co, Ni, Cu, and Mn, are effective in promoting the CRR, while Ir and Ru are efficient for the CER.[4a,d,10] These elements, positioned in the upper region of the Ellingham diagram with smaller oxidation potentials, are beneficial for forming HEAs.[7b] DFT calculations were performed to elucidate the correlation between chemical compositions in HEAs and electrocatalysis performance. Figure S1a (Supporting Information) shows the binding energy between intermediates and Mn, Fe, Co, Cu, Ni, Ru, and Ir slab models. Upon comparing binding energies between selected intermediates (*i.e.*, Li_2CO_3, $LiCO_2$, $LiCO_3$, CO_2) and the substrates (*), it is found that the element with low electronegativity exhibits the strongest binding energy with the intermediates. At the equilibrium potential of Li_2CO_3 formation (2.87 V), we observed that the CRR occurs in elements with relatively low electronegativity, such as Mn, while the CER is favored in elements with relatively high electronegativity, such as Ru and Ir (Figure S1b–e, Supporting Information). Here, we consider the following simple reaction path for CRR/CER: $* + CO_2 \rightleftharpoons *CO_2 \rightleftharpoons *LiCO_2 \rightleftharpoons *Li_2CO_3 \rightleftharpoons * + Li_2CO_3$. This path is evidenced by the energy difference observed on various metal substrates during the discharge reaction, involving CO_2 adsorption and $*LiCO_2$ reduction into $*Li_2CO_3$, as well as during the charge reaction, involving CO_2 desorption and $*Li_2CO_3$ oxidation into $*LiCO_2$. The *d*-band center on either Ru or Ir for four proposed HEAs, Ru, and Ir cluster models indicate that NiFeCoCuRu has the highest *d*-band center (−1.69), closest to the Fermi level, signifying the strong capability for the adsorption of intermediates compared with other HEAs (Figure S1f, Supporting Information).[11] It is observed that distinct adsorption behaviors between pure metals and HEAs highlight introducing HEAs offers a promising approach for the integration of diverse properties among different metals.

As a proof-of-concept, we synthesized a series of catalysts with a consistent metal ratio of 0.075 mmol (equiv. to 5 wt% loading in theory), including NiFeCoIrRu, NiFeCoMnRu, NiFeCoMnIr, and NiFeCoCuRu HEAs (referred as HEA_5/KB), Ru/KB (Ru_6/KB, equiv. to 6 wt% loading in theory), Ir/KB (Ir_{12}/KB, equiv. to 12 wt% loading in theory). Detailed synthesis methods are provided in the experimental section. Direct evidence of the successful preparation of HEA_5/KB is provided through powder X-ray diffraction (XRD), high-angle annular dark-field STEM (HAADF-STEM) results, and corresponding energy dispersive X-ray (EDX) elemental mapping images (Figures S2 and S3, Supporting Information). Our co-reduction strategy is innovative and important, especially considering previous reports that indicated challenges in synthesizing similar high-entropy materials with high loadings.[12] Additionally, a comprehensive investigation was conducted through a combination of calculations and experimental results on highly dispersed HEAs containing Ni, Fe, Co, Cu, and Ru elements in an equal molar ratio. The theoretical metal loadings range from 5 to 40 wt% on the KB supportive matrix (HEA_x/KB, x = 5, 10, 20, 30, and 40), however, the actual metal loading is observed to be lower than the corresponding theoretical values (Figure S4, Supporting Information). The observed phase segregation in XRD patterns of HEA_{40}/KB (Figure S4a, Supporting Information) and

© 2024 The Authors. Advanced Materials published by Wiley-VCH GmbH

15214095, 2024, 25, Downloaded from https://advanced.onlinelibrary.wiley.com/doi/10.1002/adma.202401288 by National Health And Medical Research Council, Wiley Online Library on [01/04/2025]. See the Terms and Conditions (https://onlinelibrary.wiley.com/terms-and-conditions) on Wiley Online Library for rules of use; OA articles are governed by the applicable Creative Commons License

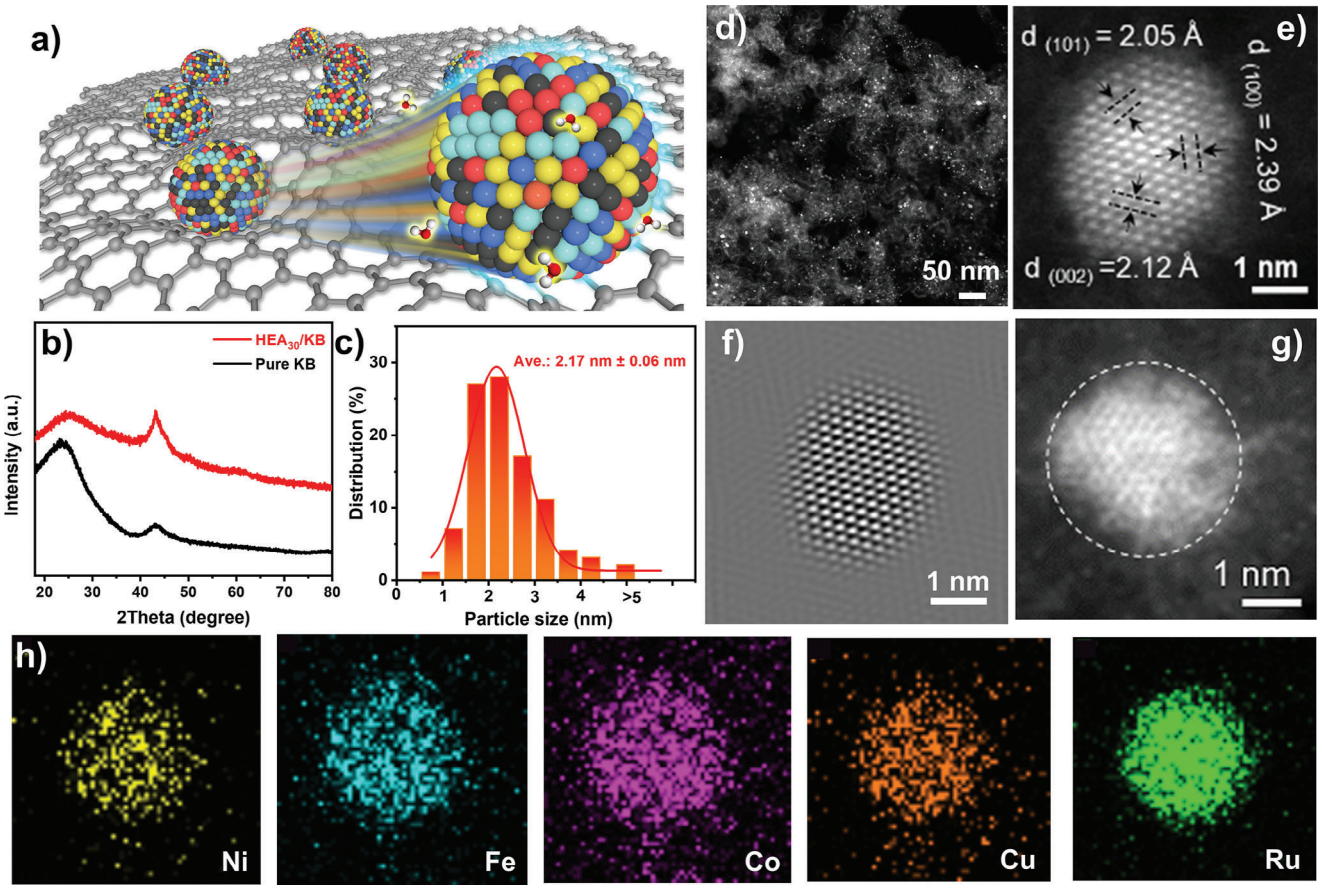

Figure 1. Characterization of NiFeCoCuRu HEA_{30}/KB material. a) Schematic representation of NiFeCoCuRu HEA_{30}/KB catalyst featuring Ni (yellow), Fe (cyan), Co (red), Cu (blue), and Ru (black) atoms encompassed by carbon surroundings. b) XRD patterns of NiFeCoCuRu HEA_{30}/KB obtained at 350 °C and pure KB. c) Histogram illustrating the size distribution of HEAs NPs within HEA_{30}/KB. d) Representative HAADF-STEM image of the NiFeCoCuRu HEA_{30}/KB. e) Atomically resolved HAADF-STEM image of a selected HEAs particle. f) Simulated crystal structure image of the selected region in (e). g) HAADF-STEM image of a chosen NiFeCoCuRu HEAs particle, and h) the corresponding EDX elemental mapping images.

NiFeCoCuRu HEA_{30}/KB with varying Ru concentrations (Figure S5, Supporting Information) respectively emphasize the importance of maintaining suitable metal loading and an equiatomic metal composition for the synthesis of HEAs/KB materials. As a result, NiFeCoCuRu HEA_{30}/KB with a metal loading of 30 wt% and equiatomic metal composition of NiFeCoCuRu alloys exhibits a desirable and stable solid-solution structure.

XRD patterns of NiFeCoCuRu HEA_{30}/KB obtained at various temperatures during calcination (Figure S6, Supporting Information) reveal a hexagonal close-packed (*hcp*) structure, similar to pure Ru metal (PDF#96-153-9053). Notably, a distinct peak observed at 43.2° in HEA_{30}/KB obtained at 350 °C, in comparison to that of pure KB, suggests a substantial increase in particle size (Figure 1b). The HEAs nanoparticles in NiFeCoCuRu HEA_{30}/KB are uniformly dispersed on the KB supports, with an average diameter of 2.17 nm (Figure 1c). This is larger than that of NiFeCoCuRu HEA_5/KB, indicating an increase in particle size with an increased metal loading, from 5 wt% to 30 wt%, as supported by HAADF-STEM images (Figure S7, Supporting Information). However, it is evident that at a high metal loading of 40 wt%, particles tend to agglomerate, resulting in larger sizes and the formation of separated phases, as confirmed by the XRD pattern (Figure S4a, Supporting Information). Figure 1d and Figure S8 (Supporting Information) illustrate the representative HAADF-STEM overview image of the NiFeCoCuRu HEA_{30}/KB loaded on the carbon support, while Figure S9 shows the microstructures of Ru_6/KB, Ir_{12}/KB and Ru_{44}/KB (equiv. to 44 wt% loading in theory). The high-resolution HAADF-STEM image in Figure 1e highlights a well-defined atomic structure of HEAs, where lattice fringes with widths of 2.39 Å, 2.12 Å, and 2.05Å correspond to the (100), (002), and (101) faces of pure Ru, respectively. The high-magnification aberration-corrected HAADF-STEM images further reveal the atomic structure of NiFeCoCuRu HEA_{30}/KB. Figure S10 (Supporting Information) indicates a characteristic atomic-resolution image of a single particle along the [002] zone axis of the NiFeCoCuRu HEA. The corresponding Fourier-filtered image and simulated crystal structure image (Figure 1f,g) reveal that the nanoparticle possesses an edge length of only 7–12 atoms. As is highlighted in Figure 1h and Figure S11 (Supporting Information), Ni, Fe, Co, Cu, and Ru elements are homogeneously distributed without apparent particle aggregation and oxidations, consistent with our XRD results. As is evidenced in the thermogravimetric analysis, there were ≈25.0 wt% alloys

© 2024 The Authors. Advanced Materials published by Wiley-VCH GmbH

15214095, 2024, 25, Downloaded from https://advanced.onlinelibrary.wiley.com/doi/10.1002/adma.202401288 by National Health And Medical Research Council, Wiley Online Library on [01/04/2025]. See the Terms and Conditions (https://onlinelibrary.wiley.com/terms-and-conditions) on Wiley Online Library for rules of use; OA articles are governed by the applicable Creative Commons License

in the NiFeCoCuRu HEA_{30}/KB (Figure S12, Supporting Information). The elemental composition ratio of Ni/Fe/Co/Cu/Ru was determined to be 18.8:18.5:20.4:20.1:22.2 (with atomic loading of 0.081:0.080:0.088:0.087:0.096 in molarity, based on weight analysis using inductively coupled plasma-atomic emission spectroscopy, Table S1, Supporting Information). These values are close to the theoretical molar ratio during the preparation.

To gain a deeper understanding of the local electronic environment of HEAs, synchrotron-based X-ray absorption fine structure measurements were conducted. The related X-ray absorption near-edge spectroscopy (XANES), extended X-ray absorption fine structure (EXAFS), and Wavelet transformed (WT) are shown in **Figure 2**. In Figure 2a, the Ru K-edge absorption threshold position in the NiFeCoCuRu HEA_{30}/KB sample slightly shifted to a negative value, accompanied by a reduced intensity of the white line. The absorption position in NiFeCoCuRu HEA_{30}/KB is even lower than that observed in the Ru foil, which indicates an electron density transfer from neighboring atoms to Ru and a change in the coordination environmental of Ru species.[7d] In contrast, the Cu, Fe, Co, and Ni K-edges in NiFeCoCuRu HEA_{30}/KB all exhibit a slight rightward shift compared with the corresponding metal reference samples (Figure 2d,g,j,m). This shift indicates electron density redistribution within HEA, which is likely attributed to the different electronegativity of these metals.[13] This is further confirmed by the Bader charge analysis of NiFeCoCuRu HEA (Figure S13, Supporting Information) and XPS results of NiFeCoCuRu HEA_{30}/KB (Figure S14, Supporting Information). The observed intensity differences within the pre-edge area and main features of the XANES spectra at Ru, Cu, Fe, Co, and Ni K-edges primarily stem from the intrinsic size effect of the ultrasmall particles rather than an oxidation effect.[14] Additionally, XANES features of the pristine *fcc* Ni K-edge and the Ni and Ru K-edge in NiFeCoCuRu HEA_{30}/KB were successfully reproduced (Figures S15 and S16, Supporting Information). This suggests that the redistribution of electrons and the fine-tuning of electronic structures occur in HEA_{30}/KB, potentially having a positive impact on the electrocatalytic activity of the catalyst when compared with pure metals. The observed white lines of Fe, Co, and Ni in Figure 2g,j,m, respectively, are close to metallic valence state, which are different from corresponding oxide reference samples. This finding suggests that Fe, Co, and Ni in the NiFeCoCuRu HEA_{30}/KB are predominantly in metallic states. The XANES spectra of Ru, along with the first-order derivatives of the XANES spectra of Cu (Figures S17–S19, Supporting Information) indicate that Ru and Cu in NiFeCoCuRu HEA_5/KB, NiFeCoCuRu HEA_{10}/KB, and NiFeCoCuRu HEA_{30}/KB exhibit metallic characteristics when compared with the respective metal references. This demonstrates that both Ru and Cu elements in these NiFeCoCuRu HEAs/KBs are in a metallic state, rather than oxidation state. However, it is noted that XANES spectra of metals in HEA_{40}/KB is different from those in other HEAs/KB, possibly indicating elemental segregation in the material.

The EXAFS results were further analyzed by fitting the Fourier transform (FT) spectra to gain a better understanding of the coordination structures of five elements in HEA_{30}/KB. Figure S20–S22 (Supporting Information) present the experimental k^2-weighted EXAFS oscillations along with the corresponding fitting curves for NiFeCoCuRu HEA_{30}/KB, metal foils, and their respective oxides at Ru, Cu, Fe, Co, and Ni K-edge. The bond structures reveal that no metal-oxygen bonds in any of the FT curves for HEA_{30}/KB, indicating that the as-synthesized NiFeCoCuRu HEA_{30}/KB is not oxidized (Figure 2b,e,h,k,n). In addition, the metal-metal distances in the first-shell of NiFeCoCuRu HEA_{30}/KB are shorter than those of the corresponding metal foils, particularly in the FT curve for Ru and Cu (Tables S2–S4, Supporting Information). The fitting results show that the average coordination numbers of the first-shell are nearly identical for all probed metals, averaging ≈6.7. The interatomic distances between Fe, Co, Ni, and Cu are consistent, measuring ≈2.50 Å, while the interatomic distance between Ru and other metals is ≈2.58 Å. This indicates that these five metallic elements form a solid-solution structure without elemental segregation in NiFeCoCuRu HEA_{30}/KB, which is consistent with XRD results. The reliability of the fitting method is supported by smaller R factors. Figure S23 (Supporting Information) further shows the overlap of all these FT curves for the first shell. The distance and amplitude are identical for the Fe, Co, Ni, and Cu absorbers, indicating that these *3d* transition metals share the same local atomic structure with a completely random mixing distribution within NiFeCoCuRu HEA_{30}/KB. In the case of Ru, the distance is slightly longer due to the larger atomic radii of Ru compared with other principal elements. Additionally, the atomic configuration of NiFeCoCuRu HEA_{30}/KB was investigated through WT analysis at metal (Ru, Cu, Fe, Co, and Ni) K-edges from EXAFS spectra (Figure 2c,f,i,l,o). No metal-metal coordination signals were observed for all those metals in HEA_{30}/KB, further confirming a solid-solution phase in HEA_{30}/KB.

The HEAs/KB materials, Ru/KB, and pure KB were used as cathode catalysts to investigate the impact of the HEAs on the reaction kinetics of Li^+-mediated CRR and CER (**Figure 3**). CV tests were initially conducted between 2.2 and 4.5 V under a pure CO_2 atmosphere (Figure 3a). The distinctive redox peaks indicate the reduction of CO_2 and the decomposition of Li_2CO_3 in the LCBs with NiFeCoCuRu HEA_{30}/KB as a catalyst. Notably, the HEA_{30}/KB cathode demonstrates a higher cathodic onset potential but a lower anodic onset potential, along with larger peak currents when compared with pure KB and Ru_{44}/KB cathodes, suggesting a significant enhancement in the kinetics of both CRR and CER. Additionally, full discharge curves (Figure S24, Supporting Information) were used to evaluate CRR kinetics and the number of active sites. The NiFeCoCuRu HEA_{30}/KB electrode exhibits a higher discharge voltage plateau of 2.85 V than pure KB (2.81 V) and Ru_{44}/KB (2.82 V), indicating excellent CRR kinetics. The HEA_{30}/KB electrode also exhibits a higher discharge capacity, signifying a larger number of accessible active sites compared with pure KB and Ru_{44}/KB.[16] To evaluate the stability of different catalysts, including NiFeCoCuRu HEA_5/KB, Ru_6/KB, Ir_{12}/KB and pure KB, long-term cycling performance was investigated at a current density of 0.1 A g^{-1} with a cut-off capacity of 1000 mA h g^{-1} (Figure S25, Supporting Information). All current densities and capacities were normalized to the mass of the catalyst. Specifically, NiCoFeCuRu HEA_5/KB exhibits a better cycling performance compared with Ir_{12}/KB, Ru_6/KB, and other HEA_5/KB with different metal compositions. This result confirms that NiCoFeCuRu HEAs is more favorable than any other HEAs for Li-mediated CRR and CER, as previously discussed in theoretical calculation results. In contrast, the pure KB cathode exhibits a limited cycling performance of 1000 h with poor

© 2024 The Authors. Advanced Materials published by Wiley-VCH GmbH

15214095, 2024, 25, Downloaded from https://advanced.onlinelibrary.wiley.com/doi/10.1002/adma.202401288 by National Health And Medical Research Council, Wiley Online Library on [01/04/2025]. See the Terms and Conditions (https://onlinelibrary.wiley.com/terms-and-conditions) on Wiley Online Library for rules of use; OA articles are governed by the applicable Creative Commons License

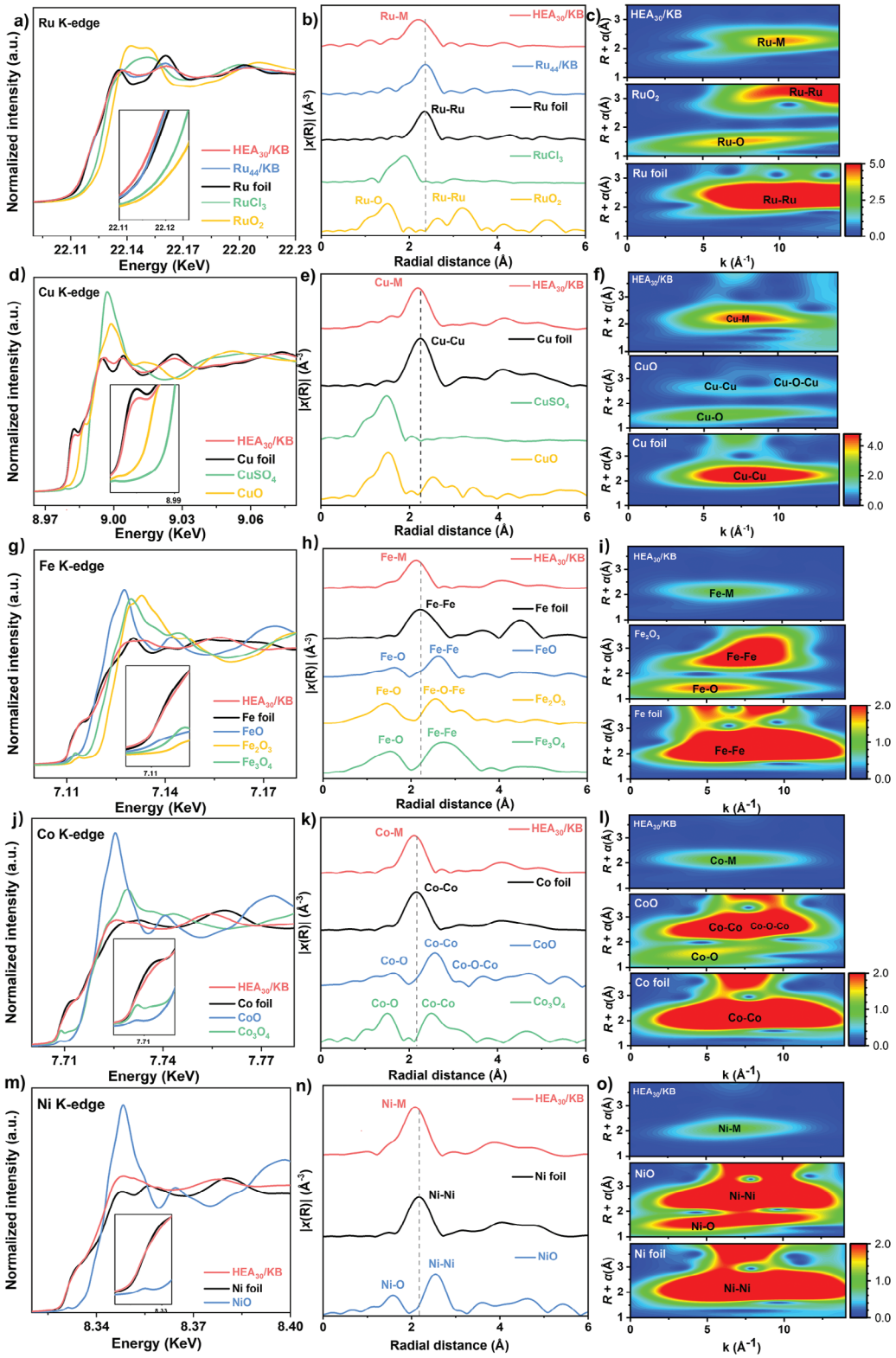

Figure 2. Atomic structure understanding of NiFeCoCuRu HEA_{30}/KB material. a,d,g,j,m) X-ray absorption near edge structure (XANES) spectra of the Ru, Cu, Fe, Co, and Ni K-edge. b,e,h,k,n) Fourier transform (FT) of Ru, Cu, Fe, Co, and Ni K-edge extended X-ray absorption fine structure (EXAFS) spectra. c,f,i,l,o) Wavelet transformed (WT) of the Ru, Cu, Fe, Co, and Ni k^3-weighted EXAFS signals.

© 2024 The Authors. Advanced Materials published by Wiley-VCH GmbH

15214095, 2024, 25, Downloaded from https://advanced.onlinelibrary.wiley.com/doi/10.1002/adma.202401288 by National Health And Medical Research Council, Wiley Online Library on [01/04/2025]. See the Terms and Conditions (https://onlinelibrary.wiley.com/terms-and-conditions) on Wiley Online Library for rules of use; OA articles are governed by the applicable Creative Commons License

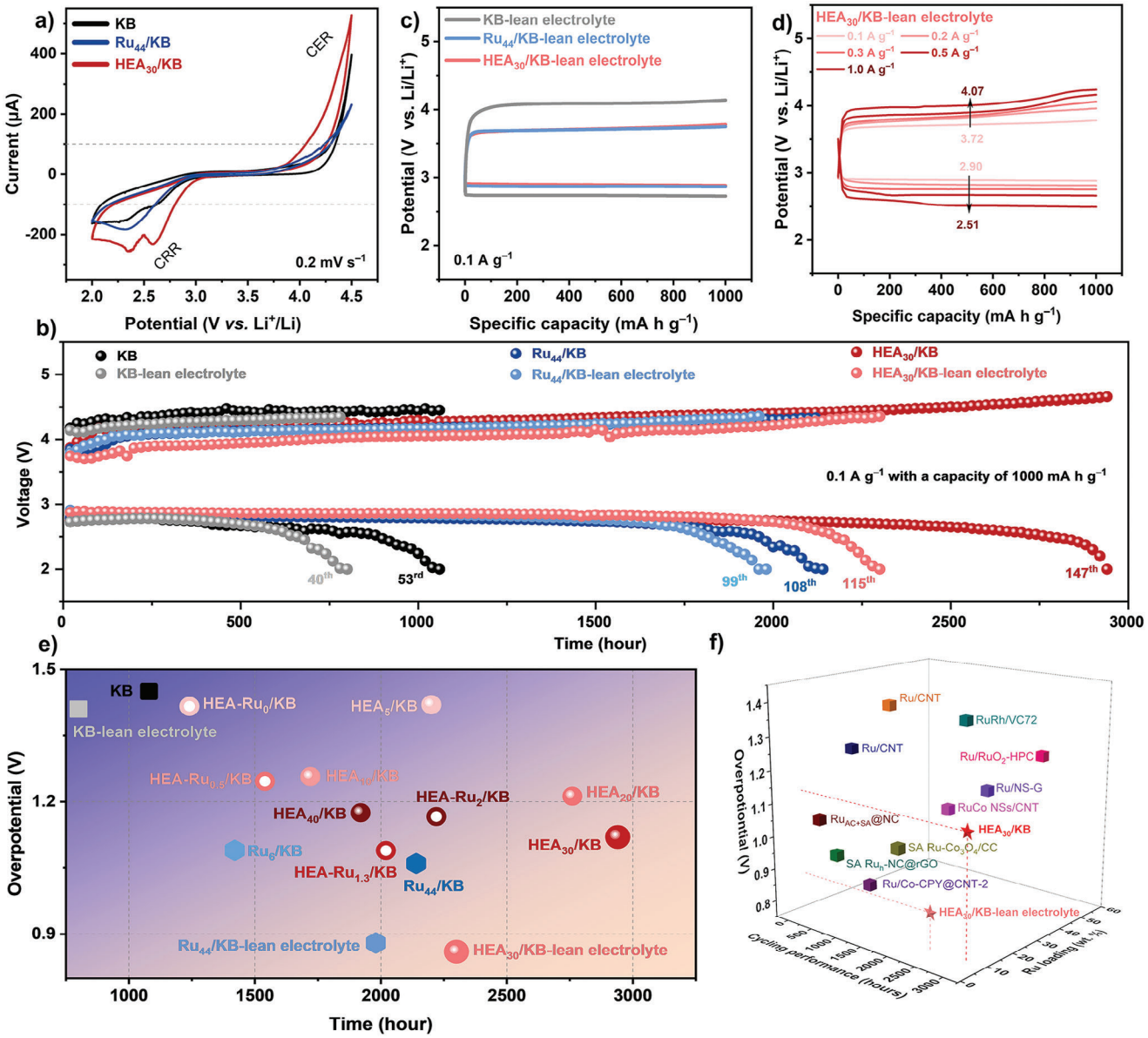

Figure 3. a) Cyclic voltammetry (CV) curves at 0.2 mV s^{-1}. b) Long cyclic performance and the corresponding discharge–charge profiles of pure KB, Ru_{44}/KB, and HEA_{30}/KB catalysts at a current density of 100 mA g^{-1} with a capacity of 1000 mA h g^{-1}. c) Charge and discharge curves for pure KB, Ru_{44}/KB, and HEA_{30}/KB with lean electrolyte at a current density of 100 mA g^{-1} with a capacity of 1000 mA h g^{-1}. d) Charge and discharge curves for HEA_{30}/KB with lean electrolyte at different current densities. e) A summary of the 1st cycle overpotential and corresponding long-term cycling stability of the as-synthesized catalysts in this work. f) Cycling performance of cathodes versus Ru loading on catalysts reported in recent literatures.[10c,15] The electrolyte dosage for batteries with lean electrolyte is 80 μL, while it is 100 μL for any other batteries.

voltage stability. The HEA_{30}/KB catalyst further demonstrates a significantly longer lifespan compared with that of pure KB, with around two times improvement in cycle life (2940 h) under the same testing conditions. This performance also outperforms the battery using Ru_{44}/KB catalyst, which lasted only 2160 h. Compared with other HEAs with different metal compositions (Figures S26 and S27, Supporting Information), the excellent rate and durable cycling performance of NiCoFeCuRu HEA_{30}/KB likely result from the strong structural stability, more accessible active sites, and intrinsic chemical activity, driven by the configurational entropy effect of ultra-small particles. This configuration promotes a high activity in electron transfer on the surface and minimizes parasitic reactions, enabling ultra-long cycling performance.

Additionally, batteries with lean electrolyte (80 μL) and thinner separators were designed to explore the correlation between cell configurations and performance optimization. As is shown in Figure 3c, the narrow median discharge-charge voltage of NiFeCoCuRu HEA_{30}/KB (0.82 V) indicates a low overpotential value than that of Ru_{44}/KB (0.84 V), significantly smaller than that of the pure KB electrode (1.36 V). Rate performances were further used to evaluate the reaction kinetics. Figure 3d indicates that,

© 2024 The Authors. Advanced Materials published by Wiley-VCH GmbH

1521 4095, 2024, 25, Downloaded from https://advanced.onlinelibrary.wiley.com/doi/10.1002/adma.202401288 by National Health And Medical Research Council, Wiley Online Library on [01/04/2025]. See the Terms and Conditions (https://onlinelibrary.wiley.com/terms-and-conditions) on Wiley Online Library for rules of use; OA articles are governed by the applicable Creative Commons License

1521 4095, 2024, 25, Downloaded from https://advanced.onlinelibrary.wiley.com/doi/10.1002/adma.202401288 by National Health And Medical Research Council, Wiley Online Library on [01/04/2025]. See the Terms and Conditions (https://onlinelibrary.wiley.com/terms-and-conditions) on Wiley Online Library for rules of use; OA articles are governed by the applicable Creative Commons License

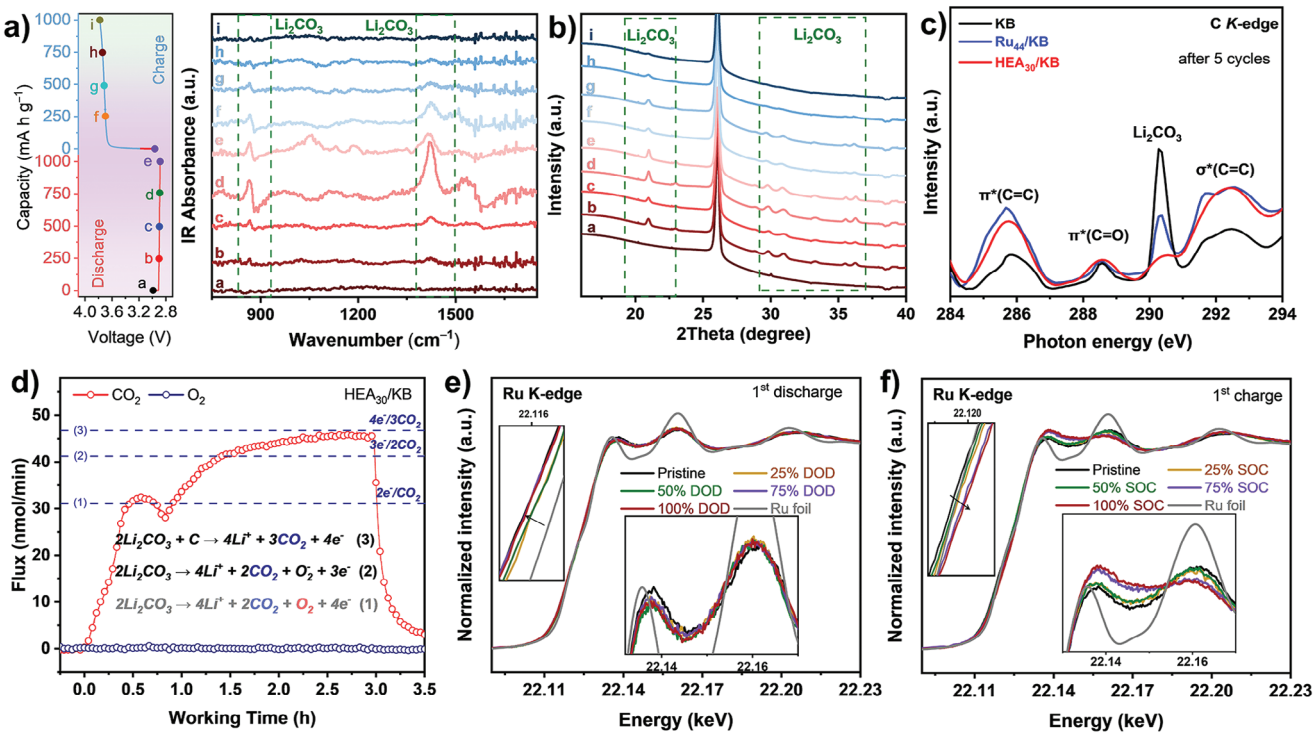

Figure 4. Electrochemical mechanism characterization of HEA_{30}/KB catalyst. a) Ex situ Fourier transform infrared (FTIR) spectra during the 1st charge/discharge curve at a current density of 100 mA g^{-1} with a cut-off capacity of 1000 mA h g^{-1}. b) Ex situ XRD during the 1st cycle. c) C K-edge soft X-ray adsorption spectroscopy (SXAS) for the cathodes after 5 cycles in KB, Ru_{44}/KB, and HEA_{30}/KB cathodes. d) In situ differential electrochemical mass spectrometry (DEMS) data of the HEA_{30}/KB. e) and f) Ex situ normalized XANES spectra of HEA_{30}/KB recorded at different DOD and SOC: e) discharge and f) charge in fluorescence mode at the Ru K-edge.

as the current density increases from 0.1 A g^{-1} to 1 A g^{-1}, the charge voltage of the NiFeCoCuRu HEA_{30}/KB electrode remains stable, although the discharge potential polarization gradually increases, shifting the discharge medium voltage from 2.90 to 2.51 V. In contrast, both pure KB and Ru_{44}/KB exhibit higher voltage polarization at each current density (Figure S28a,b, Supporting Information). The main reason for performance degradation at higher rates is likely the physical detachment of discharge products from the electrode, leading to the loss of electrical contact.[17] Importantly, batteries with lean electrolyte feature lower charge overpotential compared with those with flooded electrolytes. This could be attributed to the lower interfacial resistance provided by the thin GF/A separator and rapid mass transfer (Figure S29, Supporting Information). The short lifespan of batteries with lean electrolytes is possibly due to irreversible side reactions on the surface of the lithium foil and the insufficient electrolyte supply caused by unavoidable parasitic side reactions (Figure S30, Supporting Information). To emphasize the advantages of the NiFeCoCuRu HEA_{30}/KB catalyst, we conducted a systematic comparison, considering overpotential, cycling performance, and the loading amount of noble metals in other representative catalysts from previous studies. As shown in Figure 3e,f and Table S5 (Supporting Information), NiFeCoCuRu HEA_{30}/KB demonstrates the longest cycling performance compared with other selected catalysts, even when considering the relatively low noble metal content (≈8.8 wt%) used in the NiFeCoCuRu HEA_{30}/KB catalyst.

To understand the underlying mechanisms for the enhanced performance of both CRR and CER in HEA_{30}/KB, we used a combination of ex situ and in situ techniques, as shown in **Figure 4**. The initial charge-discharge profiles of the battery is shown on the left in Figure 4a. From FTIR spectra, two distinct bands at 863 and 1414 cm^{-1} are observed, corresponding to Li_2CO_3 species.[18] Following the battery discharged to ≈2.8 V (point c), the existence of Li_2CO_3 was confirmed by the corresponding FTIR spectra. Upon charging, the corresponding FTIR spectra indicate a gradual decrease in the intensity of Li_2CO_3 bands, eventually disappeared when the potential reached 3.6 V. Ex situ XRD patterns (Figure 4b) further reveal the emergence of the Li_2CO_3 signal, which was easily observed during discharge. Subsequent to the charging process, the signal in the HEA_{30}/KB cathode exhibited a gradual weakening, ultimately disappearing. This result indicates that the lithium carbonate is the main discharge products, which aligns with the ex situ FTIR, Raman shifts, and TEM observations (Figures S31 and S32, Supporting Information). Additionally, Figure 4c presents the SXAS spectra at the carbon K-edge for pure KB, Ru_{44}/KB, and NiFeCoCuRu HEA_{30}/KB cathodes at the charge status after five cycles. Notably, the distinctive Li_2CO_3 peak at 290.2 eV is only observed in pure KB and Ru_{44}/KB, while NiFeCoCuRu HEA_{30}/KB shows a significantly lower intensity, indicating the presence of only a trace amount of Li_2CO_3. This result further demonstrating the excellent capability of NiFeCoCuRu HEA_{30}/KB in Li_2CO_3 decomposition. We further use the in situ differential electrochemical mass spectrometry

© 2024 The Authors. Advanced Materials published by Wiley-VCH GmbH

(DEMS) to reveal the underlying reaction paths of our proposed NiFeCoCuRu HEA_{30}/KB catalyst in the battery. In Figure 4d, the balanced CO_2 evolution rate for NiFeCoCuRu HEA_{30}/KB closely approaches the standard line ascribed with $4e^-/3CO_2$ (charge-to-mass ratio) and no detectable O_2 was observed during the charge process. This suggests that most of the electrochemical reactions proceed along a fully reversible pathway via $2Li_2CO_3 + C \rightarrow 4Li + 3CO_2 + 4e^-$. Besides, similar gas evolution rates were observed in the Ru_{44}/KB cathode (Figure S33, Supporting Information). The two results provide strong evidence that our synthesized HEA_{30}/KB works along the same electrochemical mechanism as that of Ru_{44}/KB catalysts in facilitating the CRR and CER, rather than bringing in other parasitic reactions containing electrode degradation and electrolyte decomposition. In comparison, the CO_2 evolution rate for the KB cathode (Figure S33a, Supporting Information) is significantly lower than the standard line ascribed to $2e^-/CO_2$ and the charge potential reaches ≈4.5 V. It means that the single decomposition of Li_2CO_3 is incomplete during charging with pure carbon substrates even under such a high charge overpotential, which highlights the great significance of employing active Ru-based components for enhancing aprotic Li-mediated CO_2 electrochemistry.

Conventional reaction characterizations may provide insufficient information for a comprehensive understanding of catalyst degradation during electrochemical reactions. To address this issue, we conducted ex situ XAS characterizations at different electrochemical discharging and charging states. The edge position of XAS spectra, measured at different depth of discharge (DOD) or status of charge (SOC), were compared with metal foil XAS spectra as a reference. As shown in Figure 4e,f, the dominant features, particularly the positions of the white line in Ru K-edge XANES spectra, remained consistent throughout all DOD and SOC processes. More specifically, upon discharge, the Ru absorption edge slightly shifted to lower energy compared with the pristine state, indicating that Ru gained numerous electrons, and a large number of CO_2 and discharge intermediates adsorbed on the surface of Ru sites.[7d,19] This is further evidenced by the decreased white line intensity during discharging. During charging, the Ru absorption edge shifted to higher energy compared with the pristine state, suggesting increased oxidation of the Ru surface in contact with charge intermediates and discharge products.[7d] The findings are further confirmed by corresponding FT-EXAFS spectra in Figures S34–S36 (Supporting Information). Additionally, an incomplete reversal of the Ru K-edge back to a lower oxidation state at the end of the first charge is likely a result of the structural reconstruction in HEA_{30}/KB (Figure 4f). However, this structural change occurring during the discharging and charging process is reversible, as further confirmed by the subsequent discharge-charge process (Figure S37, Supporting Information). This observation implies the high stability of the HEA_{30}/KB catalyst during the reaction. We assume that the back-and-forth changes in the interactions play a crucial role in maintaining the distinctive features of Ru in the HEA_{30}/KB. This, in turn, affects the overall stability of the HEAs nanoparticles in both CRR and CER reactions. Notably, the XANES (Figure S38, Supporting Information) and FT-EXAFS spectra (Figures S39–41, Supporting Information) of the Cu K-edge follows the same trend as that of Ru K-edge, which also illustrates that Cu sites are also active sites in our HEA_{30}/KB catalyst. The above ex situ XAS results show that both Ru and Cu are active sites, which boost CRR and CER together. The XAS investigations confirm the remarkable stability of both Ru and Cu during the electrochemical processes, providing valuable insights into the factors responsible for the outstanding catalytic activity of the HEAs.

To gain a deeper insight into the performance enhancement of the HEA_{30}/KB catalyst, we conducted additional calculations, as shown in **Figure 5**. We calculate the adsorption energies of Li, C, CO_2, Li_2CO_3 and possible intermediates (CO and $Li_2C_2O_4$) on the Ru cluster and the NiFeCoCuRu HEAs. It is important to note that HEAs provide multiple adsorption sites with variations of energies compared with Ru, as shown in Figure S42 (Supporting Information), in which Li-based and C-based compounds have their preferred sites for the adsorption. In addition, compounds with large structure will have interactions with different atoms on the surface, in which HEAs with a heterogenous composition provide unique individual sites. Notably, the comparison of adsorption energies in the most stable sites for different C-based and Li-based compounds (Figure 5a) reveals that the HEAs can provide active sites for adsorption with lower E_{ads} for Li, Li_2CO_3 and $Li_2C_2O_4$ as well as C and CO. However, the adsorption of CO_2 has lower E_{ads} on Ru with a homogenous composition on the surface than that on HEAs.

To better understand the catalytic activity of multicomponent HEAs in comparison to Ru, we further conducted calculations to determine the free energies of intermediates. We consider all the possible intermediates during CER/CRR, such as the formation of Li_2CO_3 and $Li_2C_2O_4$. The unit cell of the HEAs cluster comprised 84 atoms, with Ni, Fe, Co, Cu, and Ru elements in equal proportions. To align with the experimental composition, we adopted a Ni/Fe/Co/Cu/Ru ratio of 1:1:1:1:1 for simulations and optimized configurations using the multi-cell Monte Carlo of $(MC)^2$ code. The free energies of intermediates involved in three reaction paths on both HEAs and Ru were performed under two sets of conditions: one with U = 0 V and another at the theoretical equilibrium potential of Li_2CO_3 formation ($U = U_0 = 2.87$ V). The CRR process can be assigned into two stages: first, the formation of $*Li_2CO_3$ and *CO (representing the catalytic surface) intermediates, and second, the formation of $*Li_2CO_3$ and *C. The results are illustrated in Figure 5b and Figure S43–S46 (Supporting Information), and the corresponding free energy changes for each reaction step are summarized in Table S6 (Supporting Information). From all the possible sites considered in this study, as shown in Figure S42 (Supporting Information), it is revealed that active sites containing high concentration of Ru and Ni gives higher preference for Li adsorption (sites 17, 12, 18), also with the combination of Co, Cu, Fe and Ni (site 2) gives a comparable Li adsorption energy. Whereas, the C adsorption prefers to occur in the active sites containing high concentration of Co and Fe (sites 15, 10, 2), also with the combination of Ru and Ni (site 8) gives a thermodynamically stable C adsorption. This reveals the complexity to fully understand the effect of surface composition on the adsorption process, since sub-surface composition is also another critical factor for determining the electrochemical response of HEA surface.[20] It is important to note that the intermediates are made of molecules and not just a single atom. As shown in Figure S44 (Supporting Information), it is evident that Ru is not the only element binding the intermediates on the

© 2024 The Authors. Advanced Materials published by Wiley-VCH GmbH

15214095, 2024, 25, Downloaded from https://advanced.onlinelibrary.wiley.com/doi/10.1002/adma.202401288 by National Health And Medical Research Council, Wiley Online Library on [01/04/2025]. See the Terms and Conditions (https://onlinelibrary.wiley.com/terms-and-conditions) on Wiley Online Library for rules of use; OA articles are governed by the applicable Creative Commons License

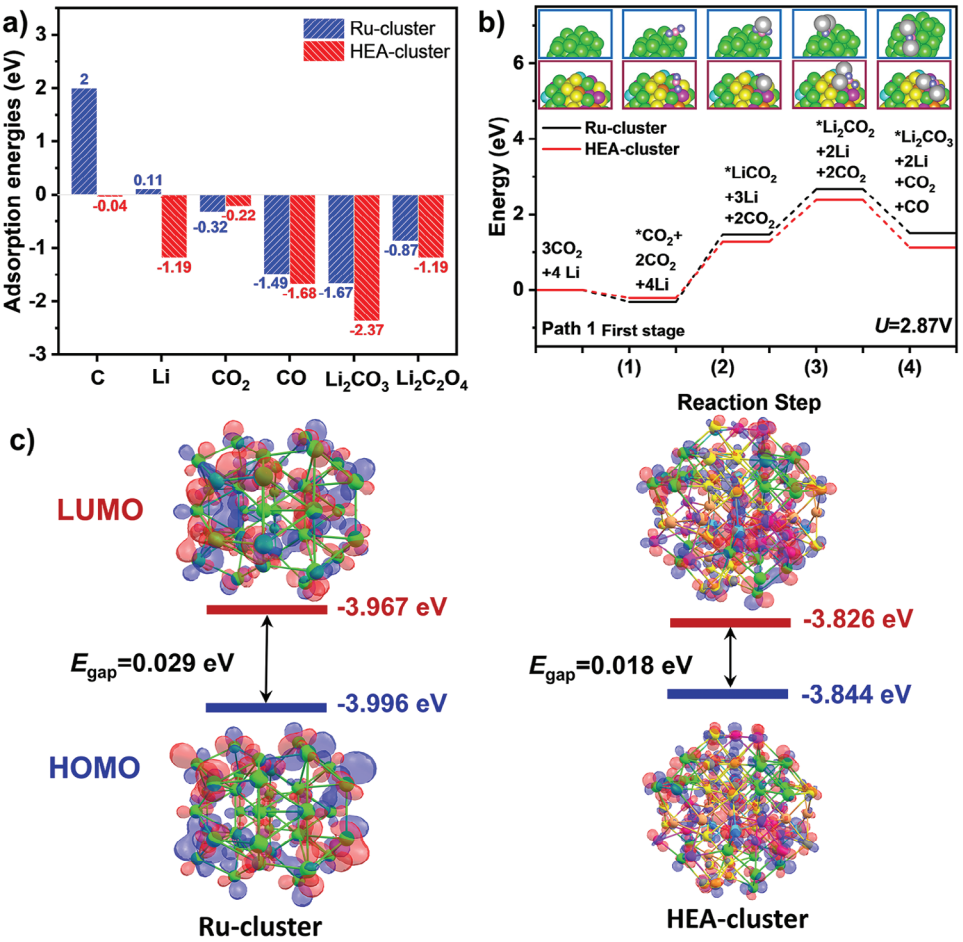

Figure 5. a) The adsorption energies for C, Li, CO_2, CO, Li_2CO_3, and $Li_2C_2O_4$ species. Statistical studies for C & Li adsorption, then only pick the most stable adsorption for derived compounds, such as CO_2, CO, Li_2CO_3, and $Li_2C_2O_4$. b) A free energy diagram of Ru-cluster and HEAs-cluster under the equilibrium potentials of $Li^+|Li_2CO_3$. c) Optimized ground state geometries and adsorption energies, energies of the Highest Occupied Molecular Orbital (HOMO) and the Lowest Unoccupied Molecular Orbital (LUMO) of Ru-cluster and HEAs-cluster. The elemental delineations in this figure are distinguished by the following colors: C in magenta, O in purple, Li in grey, Ni in yellow, Fe in cyan, Co in pink, Cu in orange, and Ru in green.

surface, as other elements including Co and Ni also exhibit some interaction with the intermediates. This becomes further complex with the adsorption of large intermediates (e.g., $LiCO_2$ and Li_2CO_2) and/or the co-adsorption of intermediates (e.g., $LiCO_3$ + CO). Herein, we found that these intermediates may adsorb favorably in a cluster of active sites containing Ru, Co, and Ni. The HEA surface consists of variety of elements with different affinity toward different intermediates – a behavior that cannot be replicated only by using monometallic alloys. During the discharge process (Figure 5b), Path 1 exhibits a lower energy barrier, making it the preferred pathway on both the basal planes of Ru and HEAs for Li_2CO_3 nucleation. However, HEAs exhibit a lower energy barrier of 1.49 eV than that of Ru (1.79 eV) for Li_2CO_3 nucleation, indicating that the HEAs attains the lowest Gibbs free energy changes for the controlling step and Li_2CO_3 nucleations. In the charging process, both Ru and HEAs favor Path 3 for Li_2CO_3 decomposition, while CO_2 desorption is the rate-limiting step and involves a notable energy barrier, with HEAs displaying a lower barrier of 0.22 eV compared with that of Ru (0.46 eV). These results further confirm that HEAs exhibits a lower energy barrier for both Li_2CO_3 formation (CRR) and its subsequent decomposition into CO_2 (CER) compared with Ru. Thus, HEAs sites demonstrate superior CRR/CER activity in comparison to Ru sites. We also calculated the energies of the Highest Occupied Molecular Orbital (HOMO) and the Lowest Unoccupied Molecular Orbital (LUMO) for the optimized structures to understand electrical conductivity (Figure 5c). The energy gap between these frontier molecular orbitals, denoted as $\Delta E_{H\text{-}L}$, was found to be 0.029 eV for Ru clusters and 0.018 eV for HEAs clusters. This difference indicates that the HEAs system exhibits a lower $\Delta E_{H\text{-}L}$ value compared with the Ru cluster, suggesting an enhancement in electrical conductivity. The enhanced electrical conductivity is beneficial for the rate capability in the Li-mediated CO_2 redox reactions.

3. Conclusion

We have demonstrated the use of a HEAs-containing material as an exceptional catalyst for Li-mediated CO_2 redox reaction with excellent catalytic activity and durability. The use of an ultrafast

© 2024 The Authors. Advanced Materials published by Wiley-VCH GmbH

15214095, 2024, 25, Downloaded from https://advanced.onlinelibrary.wiley.com/doi/10.1002/adma.202401288 by National Health And Medical Research Council, Wiley Online Library on [01/04/2025]. See the Terms and Conditions (https://onlinelibrary.wiley.com/terms-and-conditions) on Wiley Online Library for rules of use; OA articles are governed by the applicable Creative Commons License

chemical co-reduction method results in the synthesis of HEAs nanoparticles with uniform distribution, small particle size, and high loading. X-Ray-based techniques, microscopies, and computational analysis provide insights of the atomic and electron structures as well as the microenvironment change of these HEAs. When applied as an electrocatalyst for Li-mediated CO_2 redox reactions, the NiFeCoCuRu HEA_{30}/KB catalyst exhibits a significantly lower overpotential of 0.82 V and excellent stability, enduring over 2900 h, outperforming as-synthesized Ru-based catalysts. Through extensive experiments and theoretical calculations, we identify the true active sites, the fine-tuning of electronic structure, and a synergistic effect among the five elements, all of which contribute to the remarkable CO_2 redox activity of HEA_{30}/KB. Our research introduces a novel material system for enhancing the electrochemical performance of Li-mediated CO_2 redox reactions by the efficient utilization of noble-metal-based catalysts.

Supporting Information

Supporting Information is available from the Wiley Online Library or from the author.

Acknowledgements

Financial support from the Australian Research Council (DP210101486, DE240100159, and FL210100050) is acknowledged. Part of this work was carried out at the XAS, PD, and SXR beamline at the Australian Synchrotron, ANSTO (beamtime: XAS/19416, XAS/19414, XAS/19407, XAS/20390, PD/19418, and SXR/19816). The authors acknowledge the operational support from ANSTO staff, Bruce Cowie, for synchrotron-based characterizations. B.J. is supported by a Fellowship at the University of Wollongong.

Open access publishing facilitated by The University of Adelaide, as part of the Wiley - The University of Adelaide agreement via the Council of Australian University Librarians.

Conflict of Interest

The authors declare no conflict of interest.

Author contributions

L.S. and J.Y. contributed equally to this work. L.S. conducted the experiments and drafted the original manuscript. J.Y. performed theoretical calculations and revised the manuscript. J.Y., M.Z., and N.B. performed XAS theoretical calculations. B.C. and H.J. conducted DEMS testing. J.M. and G.L. contributed to electrode characterizations and data analysis. S.Z. and Z.G. supervised the project and revised the manuscript. B.J. helped with XAS testing, and C.Z. provided valuable discussions and English editing.

Data Availability Statement

The data that support the findings of this study are available from the corresponding author upon reasonable request.

Keywords

electrocatalysts, excellent stability, high entropy alloys, Li-mediated CO_2 redox reactions

Received: January 24, 2024
Revised: March 15, 2024
Published online: April 9, 2024

[1] A. Campeau, K. Bishop, N. Amvrosiadi, M. F. Billett, M. H. Garnett, H. Laudon, M. G. Oquist, M. B. Wallin, *Nat. Commun.* **2019**, *10*, 1876.
[2] Y. Qiao, J. Yi, S. Wu, Y. Liu, S. Yang, P. He, H. Zhou, *Joule* **2017**, *1*, 359.
[3] a) J. Zhou, T. Wang, L. Chen, L. Liao, Y. Wang, S. Xi, B. Chen, T. Lin, Q. Zhang, C. Ye, X. Zhou, Z. Guan, L. Zhai, Z. He, G. Wang, J. Wang, J. Yu, Y. Ma, P. Lu, Y. Xiong, S. Lu, Y. Chen, B. Wang, C. S. Lee, J. Cheng, L. Gu, T. Zhao, Z. Fan, *Proc. Natl. Acad. Sci. U. S. A.* **2022**, *119*, 2204666119; b) B. Lu, B. Chen, D. Wang, C. Li, R. Gao, Y. Liu, R. Mao, J. Yang, G. Zhou, *Proc. Natl. Acad. Sci. U. S. A.* **2023**, *120*, 2216933120.
[4] a) Z. Zhang, X. G. Wang, X. Zhang, Z. Xie, Y. N. Chen, L. Ma, Z. Peng, Z. Zhou, *Adv. Sci.* **2017**, *5*, 1700567; b) J. Xie, Y. Wang, *Acc. Chem. Res.* **2019**, *52*, 1721; c) C. Guo, F. Zhang, X. Han, L. Zhang, Q. Hou, L. Gong, J. Wang, Z. Xia, J. Hao, K. Xie, *Adv. Mater.* **2023**, *35*, 2302325; d) C. Hu, L. Gong, Y. Xiao, Y. Yuan, N. M. Bedford, Z. Xia, L. Ma, T. Wu, Y. Lin, J. W. Connell, R. Shahbazian-Yassar, J. Lu, K. Amine, L. Dai, *Adv. Mater.* **2020**, *32*, 1907436; e) G. Tian, H. Xu, X. Wang, X. Wen, T. Zeng, S. Liu, F. Fan, W. Xiang, C. Shu, *Nano Energy* **2023**, *117*, 108863.
[5] a) D. Wu, K. Kusada, T. Yamamoto, T. Toriyama, S. Matsumura, S. Kawaguchi, Y. Kubota, H. Kitagawa, *J. Am. Chem. Soc.* **2020**, *142*, 13833; b) Y. Shi, Z. Lyu, M. Zhao, R. Chen, Q. N. Nguyen, Y. Xia, *Chem. Rev.* **2021**, *121*, 649.
[6] X. Wang, D. Du, Y. Yan, L. Ren, H. Xu, X. Wen, T. Zeng, G. Tian, S. Liu, F. Fan, C. Shu, *Energy Storage Mater.* **2023**, *63*, 103033.
[7] a) Y. Yao, Z. Huang, P. Xie, S. D. Lacey, R. J. Jacob, H. Xie, F. Chen, A. Nie, T. Pu, M. Rehwoldt, D. Yu, M. R. Zachariah, C. Wang, R. Shahbazian-Yassar, J. Li, L. Hu, *Science* **2018**, *359*, 1489; b) Y. Yao, Q. Dong, A. Brozena, J. Luo, J. Miao, M. Chi, C. Wang, I. G. Kevrekidis, Z. J. Ren, J. Greeley, G. Wang, A. Anapolsky, L. Hu, *Science* **2022**, *376*, eabn3103; c) G. Feng, F. Ning, Y. Pan, T. Chen, J. Song, Y. Wang, R. Zou, D. Su, D. Xia, *J. Am. Chem. Soc.* **2023**, *145*, 11140; d) G. Feng, F. Ning, J. Song, H. Shang, K. Zhang, Z. Ding, P. Gao, W. Chu, D. Xia, *J. Am. Chem. Soc.* **2021**, *143*, 17117.
[8] a) S. G. Jung, Y. Han, J. H. Kim, R. Hidayati, J. S. Rhyee, J. M. Lee, W. N. Kang, W. S. Choi, H. R. Jeon, J. Suk, T. Park, *Nat. Commun.* **2022**, *13*, 3373; b) W. Zheng, G. Liang, Q. Liu, J. Li, J. A. Yuwono, S. Zhang, V. K. Peterson, Z. Guo, *Joule* **2023**, *7*, 2732.
[9] a) S. Gao, S. Hao, Z. Huang, Y. Yuan, S. Han, L. Lei, X. Zhang, R. Shahbazian-Yassar, J. Lu, *Nat. Commun.* **2020**, *11*, 2016; b) C. Zhan, Y. Xu, L. Bu, H. Zhu, Y. Feng, T. Yang, Y. Zhang, Z. Yang, B. Huang, Q. Shao, X. Huang, *Nat. Commun.* **2021**, *12*, 6261; c) Z. Jin, J. Lv, H. Jia, W. Liu, H. Li, Z. Chen, X. Lin, G. Xie, X. Liu, S. Sun, H. J. Qiu, *Small* **2019**, *15*, 1904180; d) Z. Chen, K. Huang, T. Zhang, J. Xia, J. Wu, Z. Zhang, B. Zhang, *Processes* **2023**, *11*, 245; e) J. K. Pedersen, T. A. A. Batchelor, A. Bagger, J. Rossmeisl, *ACS Catal.* **2020**, *10*, 2169; f) D. Du, H. He, R. Zheng, L. Zeng, X. Wang, C. Shu, C. Zhang, *Adv. Energy Mater.* **2024**, 2304238.
[10] a) J. Chen, K. Zou, P. Ding, J. Deng, C. Zha, Y. Hu, X. Zhao, J. Wu, J. Fan, Y. Li, *Adv. Mater.* **2019**, *31*, 1805484; b) X. Sun, X. Mu, W. Zheng, L. Wang, S. Yang, C. Sheng, H. Pan, W. Li, C. H. Li, P. He, H. Zhou, *Nat. Commun.* **2023**, *14*, 536; c) J. Lin, J. Ding, H. Wang, X. Yang, X. Zheng, Z. Huang, W. Song, J. Ding, X. Han, W. Hu, *Adv. Mater.* **2022**, *34*, 2200559; d) Z. Wang, B. Liu, X. Yang, C. Zhao, P. Dong, X. Li, Y. Zhang, K. Doyle-Davis, X. Zeng, Y. Zhang, X. Sun, *Adv. Funct. Mater.* **2023**, *33*, 2213931.
[11] a) J. K. Norskov, F. Abild-Pedersen, F. Studt, T. Bligaard, *Proc. Natl. Acad. Sci. U. S. A.* **2011**, *108*, 937; b) Q. Hu, K. Gao, X. Wang, H. Zheng, J. Cao, L. Mi, Q. Huo, H. Yang, J. Liu, C. He, *Nat. Commun.* **2022**, *13*, 3958.

© 2024 The Authors. Advanced Materials published by Wiley-VCH GmbH

15214095, 2024, 25, Downloaded from https://advanced.onlinelibrary.wiley.com/doi/10.1002/adma.202401288 by National Health And Medical Research Council, Wiley Online Library on [01/04/2025]. See the Terms and Conditions (https://onlinelibrary.wiley.com/terms-and-conditions) on Wiley Online Library for rules of use; OA articles are governed by the applicable Creative Commons License

[12] L. Zhao, Y. Zhang, L. B. Huang, X. Z. Liu, Q. H. Zhang, C. He, Z. Y. Wu, L. J. Zhang, J. Wu, W. Yang, L. Gu, J. S. Hu, L. J. Wan, *Nat. Commun.* **2019**, *10*, 1278.
[13] J. Hao, Z. Zhuang, K. Cao, G. Gao, C. Wang, F. Lai, S. Lu, P. Ma, W. Dong, T. Liu, M. Du, H. Zhu, *Nat. Commun.* **2022**, *13*, 2662.
[14] D. Bazin, J. J. Rehr, *J. Phys. Chem. B* **2003**, *107*, 12398.
[15] a) Z. Lian, Y. Lu, C. Wang, X. Zhu, S. Ma, Z. Li, Q. Liu, S. Zang, *Adv. Sci.* **2021**, *8*, 2102550; b) K. V. Savunthari, C. H. Chen, Y. R. Chen, Z. Tong, K. Iputera, F. M. Wang, C. C. Hsu, D. H. Wei, S. F. Hu, R. S. Liu, *ACS Appl. Mater. Interfaces* **2021**, *13*, 44266; c) J.-H. Wang, Y. Zhang, M. Liu, G.-K. Gao, W. Ji, C. Jiang, X. Huang, Y. Chen, S.-L. Li, Y.-Q. Lan, *Cell Rep. Phys. Sci.* **2021**, *2*, 100583; d) J. Cheng, Y. Bai, Y. Lian, Y. Ma, Z. Yin, L. Wei, H. Sun, Y. Su, Y. Gu, P. Kuang, J. Zhong, Y. Peng, H. Wang, Z. Deng, *ACS Appl. Mater. Interfaces* **2022**, *14*, 18561; e) Y. Xing, K. Wang, N. Li, D. Su, W.-T. Wong, B. Huang, S. Guo, *Matter* **2020**, *2*, 1494; f) S. Thoka, C. M. Tsai, Z. Tong, A. Jena, F. M. Wang, C. C. Hsu, H. Chang, S. F. Hu, R. S. Liu, *ACS Appl. Mater. Interfaces* **2021**, *13*, 480; g) Y. Qiao, J. Wu, J. Zhao, Q. Li, P. Zhang, C. Hao, X. Liu, S. Yang, Y. Liu, *Energy Storage Mater.* **2020**, *27*, 133; h) Z. Lian, Y. Pei, S. Ma, Y. Lu, Q. Liu, *ChemistrySelect* **2022**, *7*, 202104549; i) Y. Wang, J. Zhou, C. Lin, B. Chen, Z. Guan, A. M. Ebrahim, G. Qian, C. Ye, L. Chen, Y. Ge, Q. Yun, X. Wang, X. Zhou, G. Wang, K. Li, P. Lu, Y. Ma, Y. Xiong, T. Wang, L. Zheng, S. Chu, Y. Chen, B. Wang, C. S. Lee, Y. Liu, Q. Zhang, Z. Fan, *Adv. Funct. Mater.* **2022**, *32*, 2202737.
[16] B. Chen, D. Wang, J. Tan, Y. Liu, M. Jiao, B. Liu, N. Zhao, X. Zou, G. Zhou, H. M. Cheng, *J. Am. Chem. Soc.* **2022**, *144*, 3106.
[17] T. Liu, J. P. Vivek, E. W. Zhao, J. Lei, N. Garcia-Araez, C. P. Grey, *Chem. Rev.* **2020**, *120*, 6558.
[18] Y. Gu, W. W. Wang, Y. J. Li, Q. H. Wu, S. Tang, J. W. Yan, M. S. Zheng, D. Y. Wu, C. H. Fan, W. Q. Hu, Z. B. Chen, Y. Fang, Q. H. Zhang, Q. F. Dong, B. W. Mao, *Nat. Commun.* **2018**, *9*, 1339.
[19] K. P. C. Yao, M. Risch, S. Y. Sayed, Y.-L. Lee, J. R. Harding, A. Grimaud, N. Pour, Z. Xu, J. Zhou, A. Mansour, F. Bardé, Y. Shao-Horn, *Energy Environ. Sci.* **2015**, *8*, 2417.
[20] W. A. Saidi, *npj Comput. Mater.* **2022**, *8*, 86.

© 2024 The Authors. Advanced Materials published by Wiley-VCH GmbH

15214095, 2024, 25, Downloaded from https://advanced.onlinelibrary.wiley.com/doi/10.1002/adma.202401288 by National Health And Medical Research Council, Wiley Online Library on [01/04/2025]. See the Terms and Conditions (https://onlinelibrary.wiley.com/terms-and-conditions) on Wiley Online Library for rules of use; OA articles are governed by the applicable Creative Commons License